Journal of Advanced Research in Applied Sciences and Engineering Technology

Journal homepage:
https://semarakilmu.com.my/journals/index.php/applied_sciences_eng_tech/index
ISSN: 2462-1943

Comparison of PSO-Based Neural Network Predictions of F2 Ionospheric Layer Critical Frequency in Malaysia with IRI-2016

Mariyam Jamilah Homam[1,*], Noreen Nabilla Risal[1], Rohaida Mat Akir[1], Suryadi Suryadi[2]

[1] Department of Electronic Engineering, Faculty of Electrical and Electronic Engineering, Universiti Tun Hussein Onn Malaysia, 86400 Parit Raja, Batu Pahat, Johor, Malaysia
[2] Nigeria Department of Electrical Engineering, Politeknik Negeri Padang, Indonesia

ABSTRACT

This paper discussed the prediction of the ionospheric F2 layer critical frequencies, f_oF_2, at an equatorial station using a backpropagation neural network (BPNN) model in conjunction with a particle swarm optimization (PSO) algorithm, named the BPNN-PSO model, for various solar and geomagnetic activities, and compared it with the International Reference Ionosphere (IRI)-2016 model. The critical frequency data were taken from an ionosonde located at the Universiti Tun Hussein Onn Malaysia in Johor, Malaysia (1.86° N, 103.80° E). The model's outputs were analyzed using root-mean-square error (RMSE). The BPNN-PSO model outperformed the IRI-2016 model during low, medium, and high solar activity. The BPNN-PSO model had the lowest RMSE of 0.20 MHz and performed best during periods of high solar activity. This outcome was much better than the RMSE for the IRI-2016 model, which was 2.95 MHz. In addition, compared with the IRI-2016 model, the BPNN-PSO model made accurate predictions during quiet and geomagnetic storm conditions. The BPNN-PSO model had the lowest RMSE of 0.54 MHz during an intense storm, whereas the IRI-2016 model had the RMSE of 2.84 MHz during this storm.

Keywords:
Critical frequency; Ionosphere; neural network; particle swarm optimization

1. Introduction

Ionospheric parameters vary in response to space weather disturbances, which affect the performance of communication, radar, and navigation systems. The critical frequency of the F2 layer (f_oF_2) is a crucial parameter of the ionosphere. High-frequency (HF) communications forecasting has numerous critical applications, including emergency communication in disaster areas, communication with aircraft or ships, and nonline-of-sight military operations [1-2]. As a result, forecasting f_oF_2 in quiet and disturbed geomagnetic conditions is essential.

The International Reference Ionosphere (IRI), also known as an empirical model, has been the most frequently used choice for forecasting ionospheric features in the last few decades. Several researchers have attempted to establish and improve the empirical ionospheric model, for example, the IRI model, which has been gradually enhanced with new data and improved modeling

* *Corresponding author.*
E-mail address: mariyam@uthm.edu.my

https://doi.org/10.37934/araset.63.1.202218

methodologies [3-4]. Despite these advancements, various research demonstrates the neural network (NN) model's ability to improve prediction accuracy.

In 1943, Warren S. McCulloch and Walter Pitts constructed NNs by developing a computational model in their paper "A logical calculus of the ideas inherent in nerve activity." An NN is a data-driven modeling technique based on a simplified human brain function. Given its suitability for nonlinear ionospheric events, it is often utilized in forecasting f_oF_2. Numerous researchers have conducted substantial research over the last few years utilizing NNs to forecast ionospheric f_oF_2 variations under geomagnetic quiet and storm conditions. Several models for predicting ionospheric f_oF_2 have been developed [1, 5-13].

Given its numerous desirable properties, most previous studies undertaken in recent years have used a backpropagation neural network (BPNN) for forecasting ionospheric parameters. Despite these desirable features, BPNN easily slips into the local minimum without delivering a globally optimal solution due to its conceptual framework in gradient descent [9]. Thus, some researchers have used the genetic algorithm (GA) to optimize the weights of NNs and prevent the local minimum phenomena [1, 13].

1.1 Ionospheric F2 Layer Critical Frequency

The ionosphere is important in completing different daily operations; it influences radio wave propagation to distant locations on Earth [14]. The ionosphere, thermosphere, mesosphere, and exosphere comprise Earth's atmosphere. In particular, the ionosphere is a zone where solar X-rays and strong ultraviolet light ionize atoms and molecules.

This phenomenon results in the formation of numerous layers, which are denoted by the letters D, E, and F. The F layer is the most substantial region of the ionosphere for long-distance HF radio communication. The F layer has the highest concentration of charged particles and the most solar radiation. The F layer is subdivided into lower (F_1) and upper layers (F_2). F_2 has a higher density than F_1. F_2 exists during the day and at night. However, F_1 only exists during the day.

The maximum frequency limit for each ionospheric layer allows radio signals to be transmitted back to Earth and be refracted. f_oF_2 refers to the F_2 layer's maximum frequency. When a radio frequency signal is transmitted at a frequency more considerable than the critical frequency of a particular layer, the signal passes through that layer. The identical wave is refracted back to Earth when it reaches a higher critical frequency in the upper layer. Thus, the maximum refraction frequency is attained. The critical frequency, f_c is expressed as follows:

$$f_c = 9\sqrt{N_{max}}, \tag{1}$$

where f_c and N_{max} denote the critical frequency and the total electron density, respectively. The critical frequency varies with the time of day and season and the various solar trends. Abdullah and Zain [15] examined the diurnal and seasonal fluctuation of critical frequency in Malaysia. The authors determined that the trend of f_oF_2 rises gradually in the early morning, peaks at midday, and then progressively drops until late at night.

f_oF_2 is an important ionospheric parameter influenced by local time, geographic latitude, solar and magnetic activity, atmospheric wind, and other factors [16]. Substantial research has been conducted to forecast ionospheric parameters, such as f_oF_2, using a variety of methodologies [1, 5-13]. Researchers have employed empirical models, most notably the IRI model. Numerous investigations have also been conducted to assess the IRI model's ability to depict f_oF_2 parameters accurately [17-21].

Timoçin *et al.,* [17] utilized f_oF_2 data from six ionosonde stations, namely, Manila, Yamagawa, Yakutsk, Townsville, Hobart, and Terre Adelie. These stations cover all the latitudinal zones, namely, low, middle, and high latitudes with northern and southern hemispheres, and they are located around the same geographic longitude 136.0°E. The result showed the IRI-2016 performance is strongly dependent on the solar activity, latitude, season, local time, and hemisphere. For both hemispheres, the f_oF_2 values at the low-latitude station are larger than those at the middle-latitude station. The f_oF_2 values at the middle-latitude station are larger than those at the high-latitude station. The agreement between the f_oF_2 measured and IRI-2016-modeled on all stations in the northern hemisphere is best for North Summer and worst for North Winter.

Rao *et al.,* [18] compared the f_oF_2 data over the southern low-latitude station COCO (Keeling) Island for the period 2009–2013 with the IRI-2016 model. The general ionospheric trends in IRI predictions are consistent with the observation data for the diurnal, seasonal, and solar cycle variations. However, observations show a deviation in the amplitude of f_oF_2 up to the order of 5 MHz depending on local time, seasons, and phases of the solar cycle.

In addition, Rao *et al.,* [19] analyzed f_oF_2 data for the period 2008–2013 over low-latitude Chinese station at Guangzhou and compared them with the IRI-2016 model. They observed a remarkable discrepancy in f_oF_2 values in different seasons and local time variations. The IRI-2016 model underestimated the f_oF_2 values in winter and equinoxes and overestimated f_oF_2 values in summer. The IRI-modeled f_oF_2 values were greater during forenoon hours and smaller during afternoon hours than the observed f_oF_2 values.

Hong *et al.,* [20] observed f_oF_2 variations at Phu Thuy and Bac Lieu stations at Vietnam and compared them with the IRI-2016 model. The performance of IRI-2016 was worst at both stations for the high (year 2000) and low (year 2007) solar activity periods except in autumn at Bac Lieu for the low solar year.

Regarding the forecasting of the f_oF_2 values, several studies have demonstrated that NN models perform better than IRI models and researchers have shifted their focus to employing NN to predict f_oF_2 [1, 7, 10, 12, 16]. Fan *et al.,* [1] utilized Elman neural network (ENN) to predict f_oF_2 values one hour ahead at a Wuhan station. The model was optimized by the improved particle swarm optimization (IPSO) to avoid the network falling into local minimum. The prediction results of f_oF_2 showed the root mean square error (RMSE) of the ENN model was 4.30% lower than that of the BPNN model. The RMSE was further reduced by 8.92% after using the IPSO to optimize the model.

Salimov *et al.,* [7] used data from the midlatitude ionosonde in Irkutsk (Russia) for training and data from several midlatitude ionosondes, namely, Arti (Russia), Warsaw (Poland), and Mohe (China), for testing, using convolutional NNs with 2D convolution. The study resulted in correlation coefficient 0.928, RMSE 0.598 MHz, mean absolute error (MAE) 10.45%, and coefficient of determination 0.861. Yang *et al.,* [12] combined the Gray Wolf Optimization (GWO) algorithm and the attention mechanism based on the long short-term memory model to predict the f_oF_2 using the oblique ionosondes of the China Ground-based Seismo-ionospheric Monitoring Network. Their model was superior to the IRI-2016 model.

Tshisaphungo *et al.,* [16] used storm-time data during 1996-2014 from Grahamstown, South Africa ionosonde station by using NN and linear regression (LR) methods. The performances of NN and LR models were comparable during selected geomagnetic storms that fell within the data period used in modeling. However, when validated on storm outside these periods using data 19–23 December 2015 (with minimum D_{st} index of −155 nT), the NN model achieved a better performance (R = 0.62) compared with the LR model (R = 0.56).

Therefore, the purpose of this paper is to discuss the performance of a BPNN model combined with a PSO algorithm, named as the BPNN-PSO model, for the prediction of the F2 layer critical

frequency (f_oF_2) in Malaysia during various solar and geomagnetic activities. To evaluate the proposed BPNN model with the PSO algorithm, this BPNN–PSO model is compared with the IRI-2016 model.

2. Methodology

Variability in the ionospheric layer is dependent on universal time, latitude, solar and geomagnetic activity, and other factors [22]. The f_oF_2 model's input parameters are diurnal and seasonal variations, solar activity variations, and geomagnetic activity variations.

The proposed network was created using data of nine years of data collected from the Canadian Advanced Digital Ionosonde at UTHM's Advanced Telecommunications Research Centre, formerly known as the Wireless and Radio Science Centre. The current work optimized the feedforward network using PSO.

2.1 Backpropagation Neural Network

Backpropagation (BP) is a widely used approach for training artificial neural networks (ANNs) in supervised learning. Rumelhart, Hinton, and William suggested a layer-based BP algorithm [23]. BPNN has three layers: an input layer, a hidden layer, and an output layer. All nodes in one layer are connected to all nodes in the following layer. A node's weight indicates the strength of a connection. Prior to the training phase, the weight of a node is assumed random.

Each layer's nodes are connected. Through the weighted output layer relation, each input node receives a signal. The hidden layer receives data from the input layer and modifies the weights. The output layer's new value is specified. The output layer's activation function processes the hidden layer's data and generates the desired result. However, BP has considerable limitations, including a poor convergence rate and a proclivity for collapsing into the local minimum [1]. To overcome these limitations, several techniques, such as PSO [1] and genetic algorithm [10] are utilized.

2.2 Prediction Model Optimized by PSO

PSO is a computational method for describing species movement within flocks of birds or fish schools, which the algorithm simplifies and optimizes. PSO allows for the maximum utilization of potential data because each particle can learn from the findings of other particles [24]. The PSO technique is used to initialize a set of particles randomly. Each particle has three positional characteristics: position $P(m)$, velocity $V(m)$, and value of the fitness function [1]. Eq. (2) and Eq. (3) reflect the position and velocity of the ith particle in the tth iteration, respectively. Eq. (4) and Eq. (5) indicate the optimal position of each particle (i.e., the local optimum) and the optimal position of the entire population (i.e., the global optimum). Thus, the position and velocity of each particle are updated by Eq. (6) and Eq. (7), respectively. r signifies random scalars between 0 and 1 in Eq. (6). The learning variables c_1 and c_2 are set to the same value, which is typically 2 [11]. If the global optimum surpasses the predefined value or the number of iterations exceeds the limit, the PSO satisfies the criterion. Eqs. (5) and (6) were utilized to update each particle's velocity and location using the known local and global bests. The termination terms were scrutinized to determine if they had been complied with. If the prerequisites were met, PSO was halted. The NN system's input would be the most recent global best.

$$P(m) = (p_1(m), p_2(m)) \ldots p_k(m)), \tag{2}$$

$$V(m) = (v_1(m), v_2(m))\ldots v_k(m)), \tag{3}$$

$$P_{best} = (p_1, p_2 \ldots p_t), \tag{4}$$

$$G_{best} = (g_1, g_2 \ldots g_t), \tag{5}$$

$$V_i(m+1) = V_i(m) + c_1 r(P_{best} - P_i(m) + c_2 r(G_{best} - P_i(m), \tag{6}$$

$$P(m+1) = P_i(m) + V_i(m+1). \tag{7}$$

Figure 1 illustrates the BPNN-PSO flowchart and specifies the position as $P_i(m)$ and the velocity of each particle as $V_i(m)$. Three elements affect particle motion: the weight of inertia (i_w), the acceleration in the local system (C_1), and the inertia of the system (C_2).

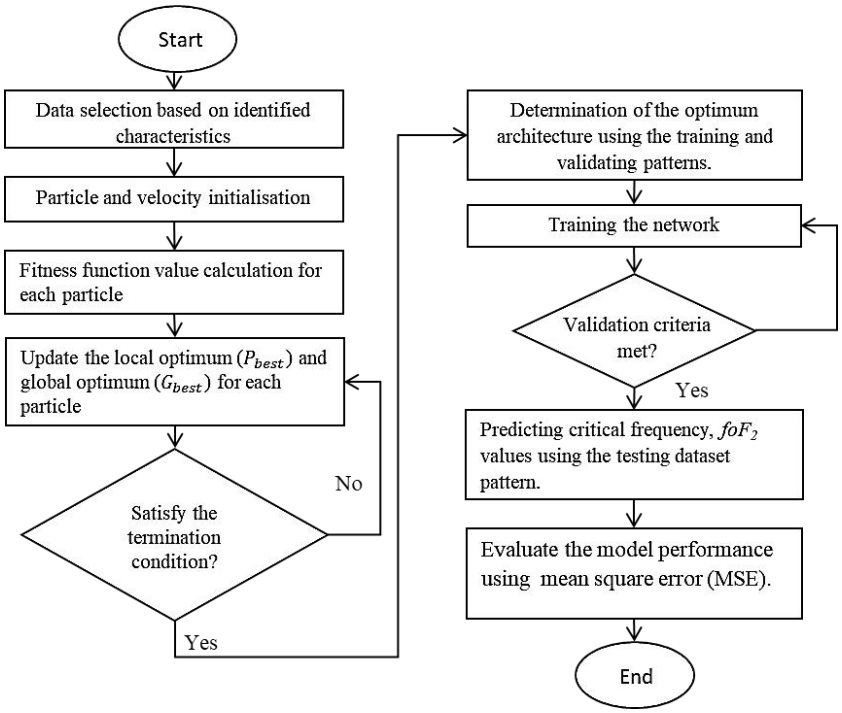

Fig. 1. Flowchart of BPNN-PSO

2.3 Inputs to the Prediction Model

The data selection method was carried out using eight input parameters to represent diurnal and seasonal variations, solar activity variations, and geomagnetic activity variations. These input parameters are the day number (DN), universal time (UT), sunspot number (SSN), solar flux F10.7, geomagnetic activity index (K_p), and disturbance storm time (D_{st}), which were employed throughout the training phase.

2.3.1 Diurnal and seasonal variations

Diurnal and seasonal variations were represented by UT values ranging from 0000 to 2300 UT and DN values ranging from 1 to 365. The sine and cosine of UT and DN were converted into quadratic components presented in Eq. (8) until Eq. (11) [1].

$$UTS = \sin\left(\frac{2\pi \times UT}{24}\right) \quad (8)$$

$$UTC = \cos\left(\frac{2\pi \times UT}{24}\right) \quad (9)$$

$$DNS = \sin\left(\frac{2\pi \times DN}{365}\right) \quad (10)$$

$$DNC = \cos\left(\frac{2\pi \times DN}{365}\right) \quad (11)$$

2.3.2 Solar variations

Solar activity was determined using the SSN and solar flux F10.7 acquired from the NASA/Goddard Space Flight Center Physics Data Facility. SSN and solar flux F10.7 were classified into three phases based on their solar activity: low, medium, and high. Table 1 shows the yearly mean of SSN, solar flux F10.7, and solar activity level from January 2004 to December 2012. Figure 2 illustrates the daily SSN and solar flux for the same periods.

Table 1
Yearly mean of SSN and solar flux F10.7 from January 2004 to December 2012

Year	Mean SSN	Mean solar flux F10.7	Solar activity level
2004	65.34	106.49	High
2005	45.71	91.71	Medium
2006	24.67	79.99	Medium
2007	12.64	73.07	Low
2008	4.15	74.16	Low
2009	4.76	70.54	Low
2010	24.90	79.99	Medium
2011	80.81	115.70	High
2012	84.39	122.29	High

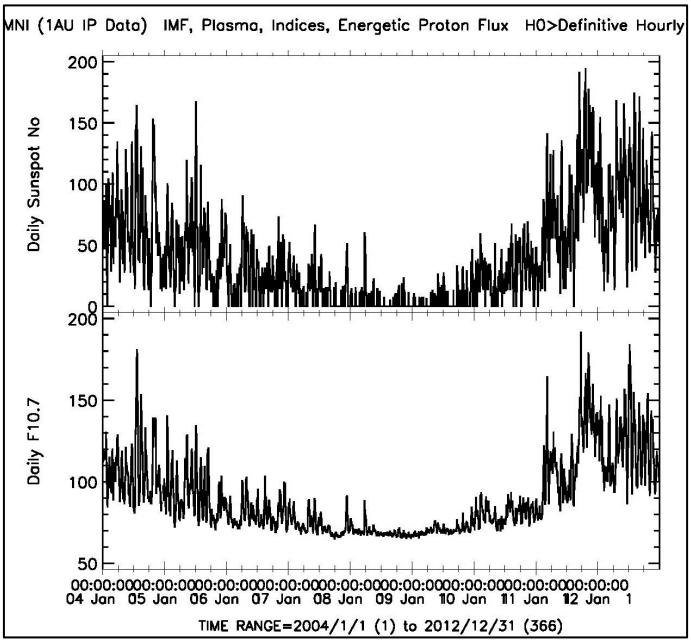

Fig. 2. Daily SSN dan solar flux F10.7 data from January

2004 to December 2012 [25]

2.3.3 Geomagnetic variations

A geomagnetic storm is a major disturbance of the Earth's magnetosphere induced by a tremendous energy flow from solar activity into the planet's atmosphere [26]. The F_2 layer's critical frequency, f_oF_2, fluctuates substantially in response to solar and geomagnetic activity. Geomagnetic indicators, such as K_p and D_{st}, indicate the presence of geomagnetic storms. Table 2 specifies the level of equatorial geomagnetic disturbance, D_{st}, during the study. Table 3 summarizes the global geomagnetic disturbance level, K_p, and its equivalent value. Figure 3 illustrates the three-hour K_p and one-hour D_{st} data from January 2004 to December 2012.

Table 2
Equatorial geomagnetic disturbance level, D_{st}

Geomagnetic disturbance level	D_{st} (nT)
Quiet condition	Peak $D_{st} >- 20$
Weak storm	Peak $D_{st} >- 50$
Moderate storm	$-100 < peak\ D_{st} <- 50$
Intense storm	Peak $D_{st} <- 100$

Table 3
Global geomagnetic disturbance level, K_p

Geomagnetic disturbance level	K_p index	Equivalent K_p index
Quiet condition	0–4	3–43
Weak storm	5	47–53
Moderate storm	6–7	57–73
Intense storm	8–9	77–93

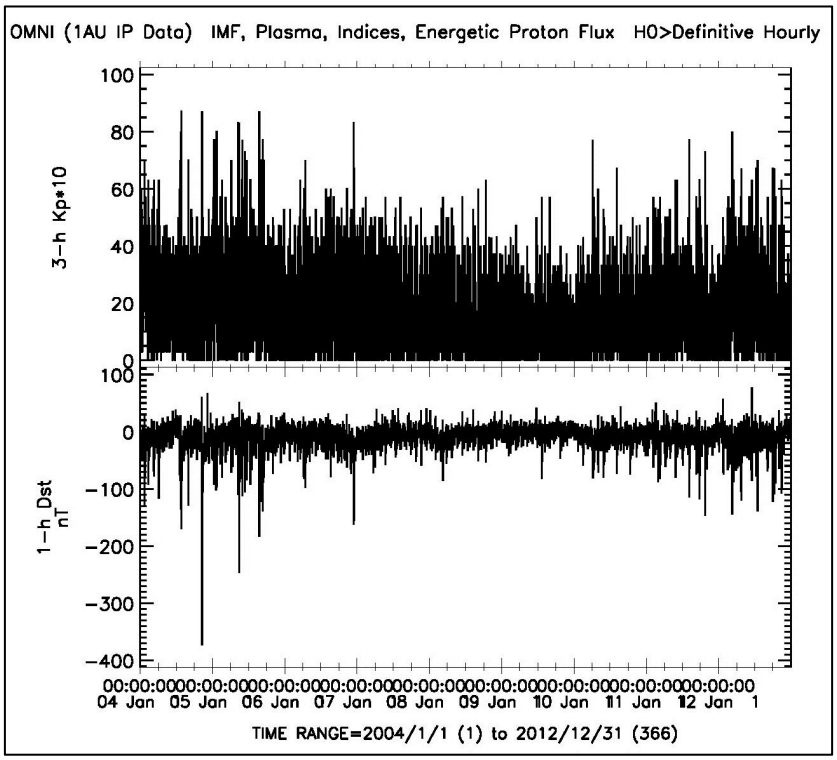

Fig. 3. 3-hour K_p and 1-hour D_{st} data from January 2004 to December 2012 [25]

2.4 Training, Validation, and Testing Phases

The raw ionogram data were manually scaled to provide the output for the BPNN-PSO model, which is the f_oF_2. The data were split into two sets: training and testing datasets. The training data period ranged from 2004 to 2012. The input ranges for the solar and geomagnetic activities in Table 4 indicate a wide range of activity levels to represent many solar and geomagnetic activities. Table 5 shows the training parameter settings for the model. The number of hidden layers and hidden neurons were chosen based on a few trials during the training phase.

Table 4
Input ranges of the training dataset

Parameter	Range
SSN	0 to 167
Solar flux F10.7	70.7 to 170.4
K_p index	0 to 87
D_{st} index (nT)	−320 to 30

Table 5
Settings for training parameters for BPNN-PSO

Parameter	Setting
Number of training data	10500
Number of hidden layers	2
Number of hidden neurons	11
Training function	TRAINLM
Adaption learning function	LEARNGDM
Transfer function	TANSIG
Performance function	MSE

Tables 6 and 7 show the testing dataset period. The testing datasets were not included in the training and validation phases. The testing datasets in Table 6 were used to examine the performance of the BPNN-PSO models over a range of solar activities. The months were chosen to represent low, medium, and high solar activity. Table 7 provides the testing datasets on selected dates to compare the performance of the BPNN-PSO models under different geomagnetic conditions: quiet and storms.

Table 6
Monthly mean of SSN and solar flux F10.7 for testing dataset

Month/year	Mean SSN	Mean solar flux F10.7	Solar activity level
May 2008 and April 2009	8.39	71.22	Low
November 2004 and May 2005	44.72	93.00	Medium
October 2011 and January 2012	110.00	146.71	High

Table 7
Range and mean of SSN diurnally under quiet and geomagnetic storm conditions and its Dst and Kp

Month/year	Geomagnetic condition	D_{st} range (nT)	Equivalent K_p range
14 August 2004, 4 March 2011, and 28 March 2011	Quiet	−27 to 10	0 to 33
2 March 2008, 9 March 2008, and 10 March 2008	Moderate storm	−86 to −16	17 to 57
8 November 2004, 11 November 2004, and 15 May 2005	Intense storm	−374 to −40	13 to 97

2.5 Error Analysis

The test dataset was used to assess the final output of the BPNN-PSO models during the training phase. During the testing phase, the test dataset was utilized to evaluate the final output of the BPNN-PSO model. The root-mean-square error (RMSE) was used to evaluate the model's performance by using the measured f_oF_2, f_{obs}, and the modeled f_of_2, f_{pre}.

$$RMSE = \sqrt{\frac{1}{N}\sum_{i=1}^{n}\left(\overline{f_{obs}} - \overline{f_{pre}}\right)^2} \quad (12)$$

2.6. IRI-2016 Parameters

The IRI-2016 model required several inputs, including location, time, and date. Other optional inputs can also be included. With these inputs, the IRI-2016 model provided the electron density values from which the critical frequency f_oF_2 can be extracted. Then, RMSEs were calculated by using the measured f_oF_2 and the modelled f_oF_2.

3. Results

3.1 Testing Result During Low, Medium, and High Solar Activity

Table 8 summarizes the prediction results of the BPNN-PSO and IRI-2016 models for years of low, moderate, and high solar activity. The forecast results for the output of BPNN-PSO models in the table correspond to those conducted by Zhao *et al.,* [10], where f_oF_2 was forecasted using an NN with GA. The IRI-2016 model overestimated the actual value of f_oF_2. The RMSE of BPNN-PSO's predictions ranged between 0.20 MHz to 0.47 MHz, whereas Zhao *et al.,* [10] revealed an RMSE of between 0.55 MHz and 2.09 MHz.

Table 8
Daily test results for low, medium, and high solar activity for the IRI-2016 and BPNN-PSO models

Solar epoch	RMSE (MHz)	
	IRI-2016	BPNN–PSO
Low solar activity	3.05	0.25
Medium solar activity	2.84	0.47
High solar activity	2.95	0.20

The RMSE of the BPNN-PSO model was lower than that of the IRI-2016 model. The IRI-2016 model's RMSE was between 2.84 MHz and 3.05 MHz. The BPNN-PSO model surpassed the IRI-2016 model with a smaller RMSE. These findings were consistent with the findings by Fan *et al.,* [1], which claimed BPNN with PSO had higher prediction accuracy than the IRI model. Figure 4 illustrates the observed f_oF_2 and the models' predictions during periods of low solar activity.

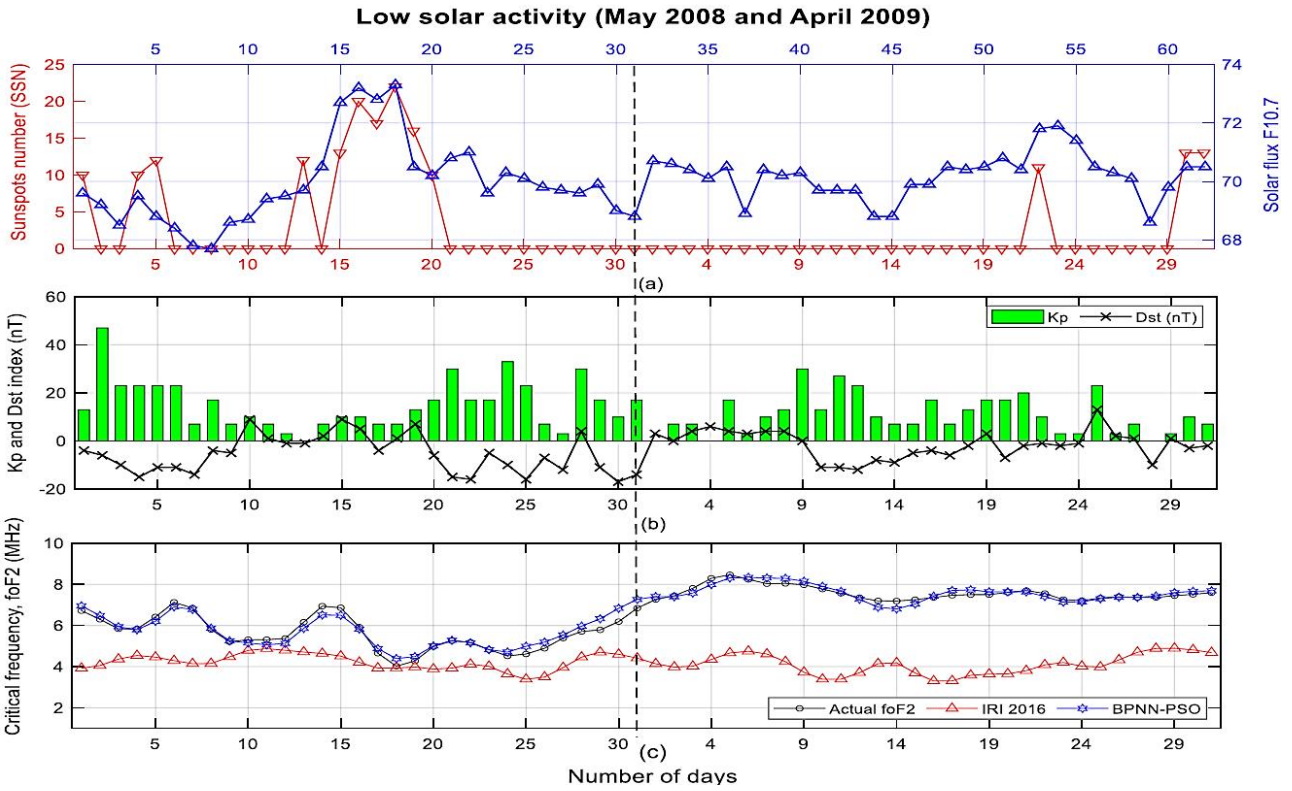

Fig. 4. Comparison of actual f_oF_2 and the models' predictions during low solar activity (May 2008 and April 2009) (a) Daily SSN and solar flux F10.7 (b) D_{st} and equivalent K_p indices (c) Actual (black), IRI-2016 (red), and BPNN-PSO (blue)

The BPNN-PSO model outperformed the IRI model during low solar activity, with an RMSE of 0.25 MHz compared with 3.05 MHz for the IRI model. The larger the RMSE was, the less accurate the prediction became. The BPNN-PSO model outperformed the IRI-2016 model in general. The BPNN–PSO model's forecast mirrored the trend of the actual value. The BPNN-PSO forecast was accurate for most data points.

On 5 May 2008, the BPNN-PSO model predicted f_oF_2 of 6.21 MHz, which was close to the actual value of f_oF_2 of 6.42 MHz. The IRI-2016 model underestimated f_oF_2's actual value by providing f_oF_2 of 4.46 MHz. On 20 May 2008, the BPNN-PSO model predicted f_oF_2 4.96 MHz. This value was closer to the actual value of 5.01 MHz than the IRI-2016 model, which predicted a decrease of f_oF_2 at only 3.88 MHz.

Figure 5 compares the predictions of the BPNN-PSO and IRI-2016 models during periods of moderate solar activity. Although the geomagnetic storms occurred on 8 November 2004, both models adequately fit the rising and falling regions of the f_oF_2 curve during periods of moderate solar activity. The RMSE for the BPNN-PSO model was 0.47 MHz, whereas that for IRI-2016 was 2.84 MHz. On 8 November 2004, D_{st} and equivalent K_p values were -343 nT and 83 (K_p= 8^+), respectively, thus indicating an intense storm. The BPNN-PSO model predicted 4.39 MHz, an improvement of 40.67% over the IRI-2016 prediction, which overpredicted the actual value (i.e., 4.18 MHz) of 6.09 MHz.

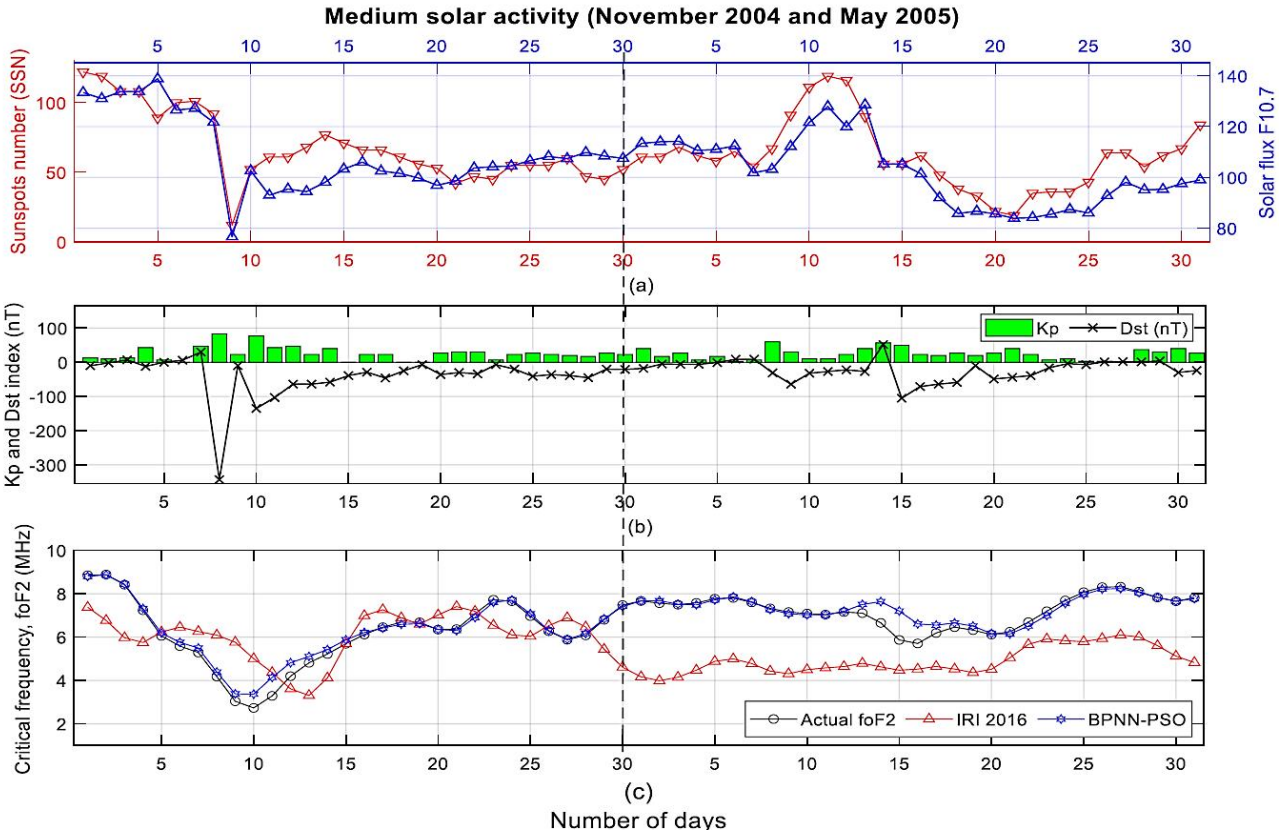

Fig. 5. Comparison of actual f_oF_2 and the models' predictions during medium solar activity (November 2004 and May 2005) (a) Daily SSN and solar flux F10.7 (b) D_{st} and equivalent K_p indices (c) Actual (black), IRI-2016 (red), and BPNN-PSO (blue)

Additionally, on 16 November 2004, the BPNN-PSO model confirmed its accuracy in forecasting during a geomagnetic storm. D_{st} and equivalent K_p values of –58 nT and 40 (K_p= 4), respectively, implied an intense storm. Compared with IRI-2016 (i.e., 4.12 MHz), the forecast of the BPNN–PSO model improved by 17.24% with 5.42 MHz. The BPNN–PSO model's prediction came closer to the actual f_oF_2 of 5.22 MHz. These findings suggested the BPNN-PSO forecast outperformed the IRI-2016 model, especially during periods of moderate solar activity.

During periods of high solar activity, the BPNN–PSO model also outperformed the IRI-2016 model. The RMSE of the BPNN-PSO model was 0.20 MHz, whereas that of the IRI-2016 model was 2.95 MHz. Figure 6 compares the actual f_oF_2 and model predictions under high solar activity. The prediction of f_oF_2 using our BPNN-PSO model provided much better result compared with the IRI-2016 model. On 20 October 2011, D_{st} and equivalent K_p were –12 nT and 7 (K_p=1), respectively. The BPNN-PSO forecast f_oF_2 of 8.23 MHz was higher than the IRI-2016 model's prediction (i.e., 7.27 MHz), which was closer to the actual f_oF_2 value (8.14 MHz). These findings revealed the BPNN-PSO model could make accurate forecasts during periods of high solar activity because it attained the lowest prediction error at each data point and increased prediction performance compared with the IRI-2016 model.

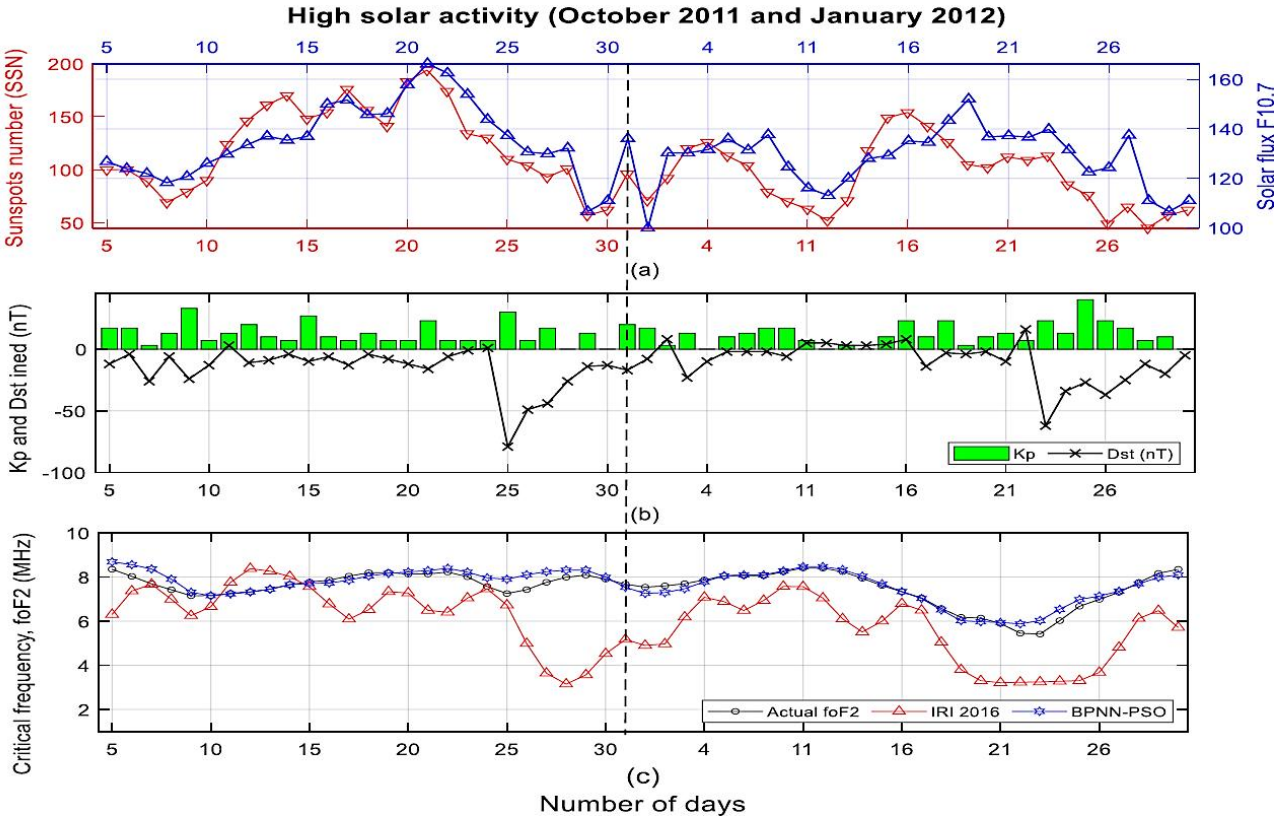

Fig. 6. Comparison of actual f_oF_2 and the models' predictions during high solar activity (October 2011 and January 2012) (a) daily SSN and solar flux F10.7 (b) D_{st} and equivalent K_p indices (c) actual (black), IRI-2016 (red), and BPNN-PSO (blue)

3.2 Testing Result During Quiet, Moderate, and Intense Storm Condition

Table 9 summarizes the diurnal testing results under quiet and geomagnetic storm conditions using both models. The IRI-2016 model's RMSE under quiet conditions was 2.72 MHz. The RMSE of the BPNN-PSO model was 0.51 MHz, which was substantially less than that of the IRI-2016 model. This finding showed that the BPNN-PSO model performed better with a smaller RMSE than the IRI-2016 model in quiet conditions.

Table 9
Diurnal testing results under quiet, moderate, and intense storm conditions for IRI-2016 and BPNN-PSO models

Solar epoch	RMSE (MHz)	
	IRI-2016	BPNN-PSO
Quiet condition	2.72	0.51
Moderate storm	3.17	0.33
Intense storm	2.84	0.54

Figure 7 compares the IRI-2016 and BPNN-PSO models' predictions with the equivalent K_p and D_{st} indices under quiet conditions. The BPNN-PSO model performed better than the IRI-2016 model in predicting the actual f_oF_2 on 14 August 2004 at 1110 UT. The BPNN-PSO model predicted 6.57 MHz, which was closer to the actual value of f_oF_2, 6.37 MHz, than the IRI-2016 model, which predicted 6.10 MHz. In addition, on 28 March 2011 at 1045 UT, the BPNN-PSO model prediction was more accurate than that of the IRI-2016 model. The model predicted 7.59 MHz, which was

0.39% closer to the actual value of f_oF_2 (i.e., 7.56 MHz). The IRI-2016 model predicted a value of 6.70 MHz, 11.36% lower than the actual value. In general, the BPNN-PSO model performed better under quiet conditions, owing to its consistently low prediction errors across all data points. The IRI-2016 model underperformed in quiet conditions due to its large error percentage.

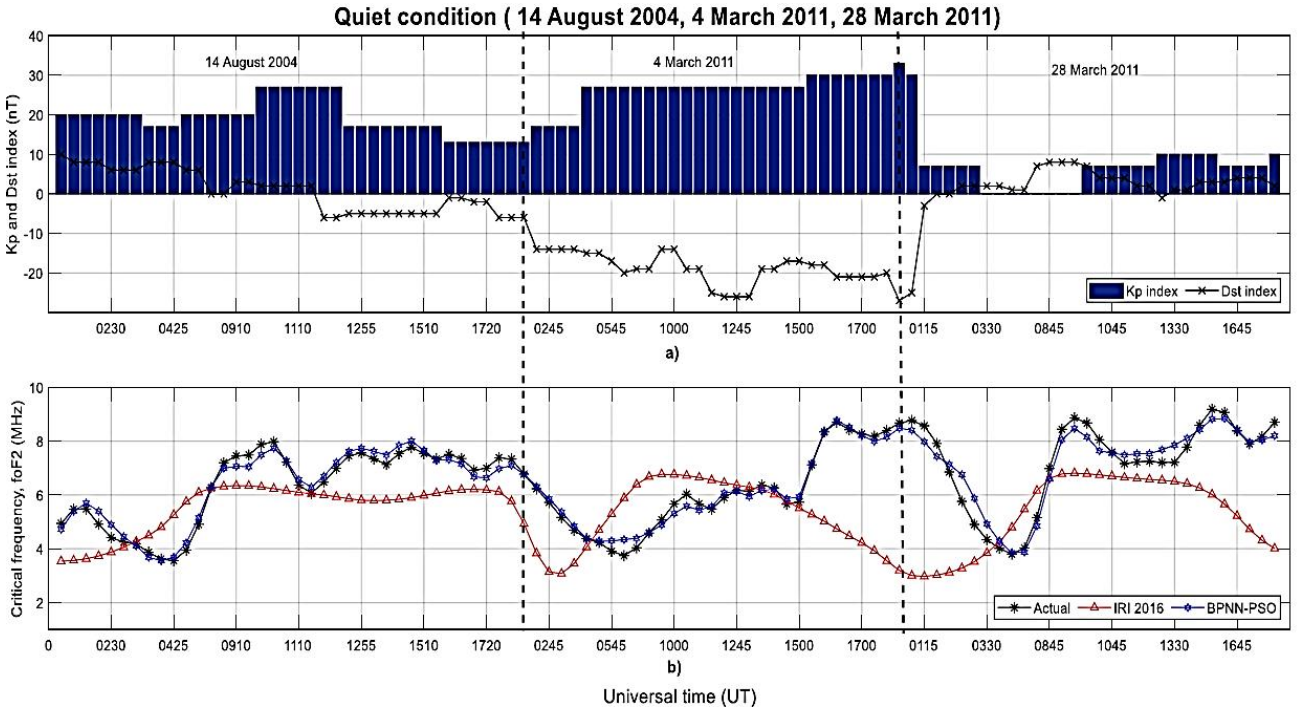

Fig. 7. Comparison of actual f_oF_2 and the models' predictions under quiet geomagnetic conditions (14 August 2004, 4 March 2011, and 28 March 2011) (a) D_{st} and equivalent K_p indices (b) Actual (black), IRI-2016 (red), and BPNN-PSO (blue)

Figure 8 compares the actual f_oF_2 and model projections during moderate storms. Table 9 shows the RMSE of the BPNN-PSO model was substantially less than that of the IRI-2016 model during moderate storms. The BPNN-PSO model had an RMSE of 0.33 MHz. The IRI-2016 model's RMSE during moderate storms was 3.17 MHz. The prediction result of the BPNN-PSO model was compatible with the model reported by Rumelhart *et al.,* [23] and Xie *et al.,* [24], in which the response of f_oF_2 to a geomagnetic storm was highly evident. The predicted f_oF_2 value decreased with the D_{st} index value, which decreased from –52 nT to –86 nT (moderate storm) between 0430 and 0930 UT on 9 March 2008. These findings corroborate studies published by Wang *et al.,* [27], which demonstrated the variance of f_oF_2 during geomagnetic storms is dependent on storm intensity.

On 2 March 2008 at 2130 UT during a weak storm, the BPNN-PSO model predicted a frequency of 6.62 MHz, which was only 0.15% difference from the actual value of f_oF_2 (6.61 MHz). The BPNN-PSO model was more accurate than the IRI-2016 model. The IRI-2016 model predicted 2.21 MHz, 66.57% higher than the actual value. However, on 9 March 2008 at 0930 UT during a moderate storm, the BPNN-PSO model overestimated the actual value of f_oF_2 by 29.31%, thus resulting in a value of 4.50 MHz, whereas the actual value was 3.48 MHz. The IRI-2016 model forecasted a value that was 18.38% lower (4.12 MHz) than the actual value. Both provided relatively higher prediction error, but IRI-2016 model provided better result at this instance. However, in general, our BPNN-PSO still provided better results during these periods.

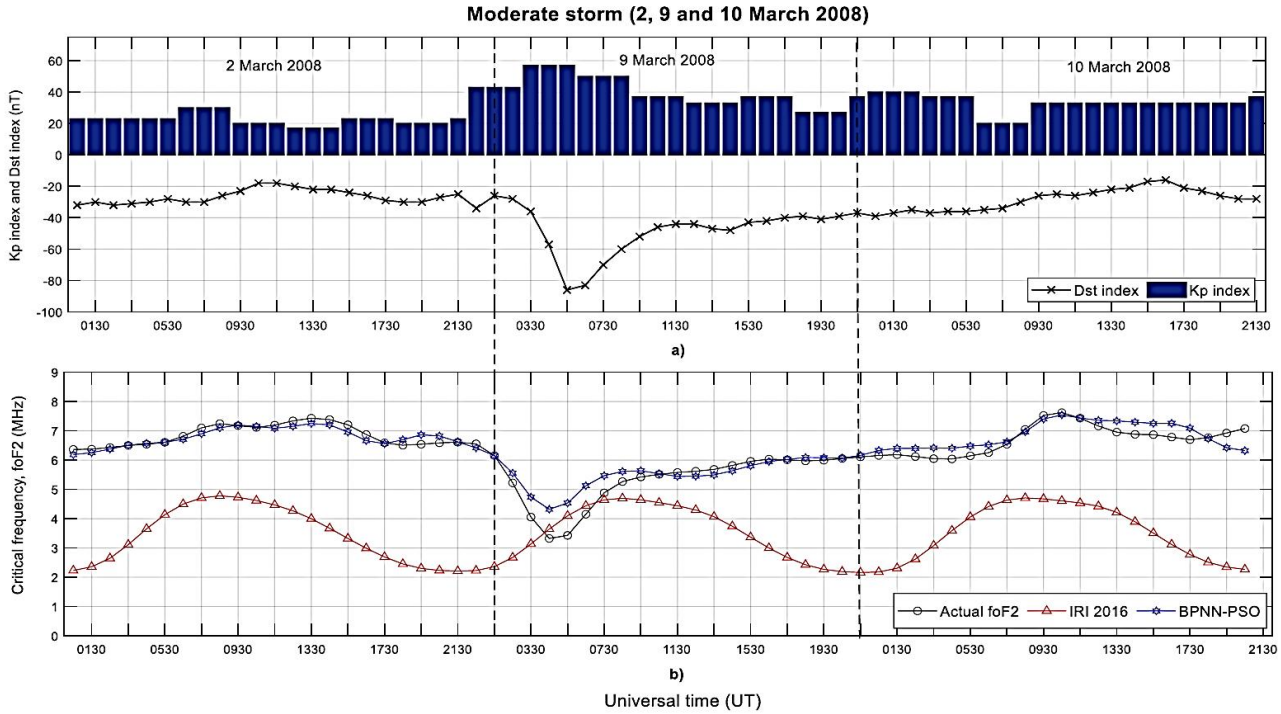

Fig. 8. Comparison of the actual f_oF_2 and the models' predictions during a moderate storm (2, 9, and 10 March 2008) (a) D_{st} and equivalent K_p indices (b) Actual (black), IRI-2016 (red), and BPNN-PSO (blue)

Figure 9 compares the actual f_oF_2 and model predictions during an intense storm. BPNN-PSO models adequately fit the rising and falling parts of the f_oF_2 curve despite the intense storms that occurred between 0000 and 2300 UT on 8 November 2004, 11 November 2004, and 25 October 2011. On 8 November 2011 at 1000 UT, with D_{st} and equivalent K_p values of –299 nT and 70, respectively, the percentage error between the BPNN-PSO prediction (f_oF_2=3.22 MHz) and the actual value of f_oF_2 (3.06 MHz) was 5.23%. The IRI-2016 model provided the f_oF_2 of 7.21 MHz, resulting in 135.62% error. In general, the BPNN-PSO model's prediction was more accurate because of its low error percentage in many cases during these periods. The RMSE of the IRI-2016 model was 2.84 MHz under intense storm conditions. The RMSE of the BPNN-PSO model was smaller than the results of the IRI-2016 model at 0.54 MHz. The BPNN-PSO prediction performed remarkably better than the IRI-2016 model during an intense storm, owing to its smaller error percentage. The results corroborated those found by Timoçin *et al.,* [28], which concluded that the NN model is critical for developing an ionospheric storm forecasting system because it can predict the presence of such severe disturbances.

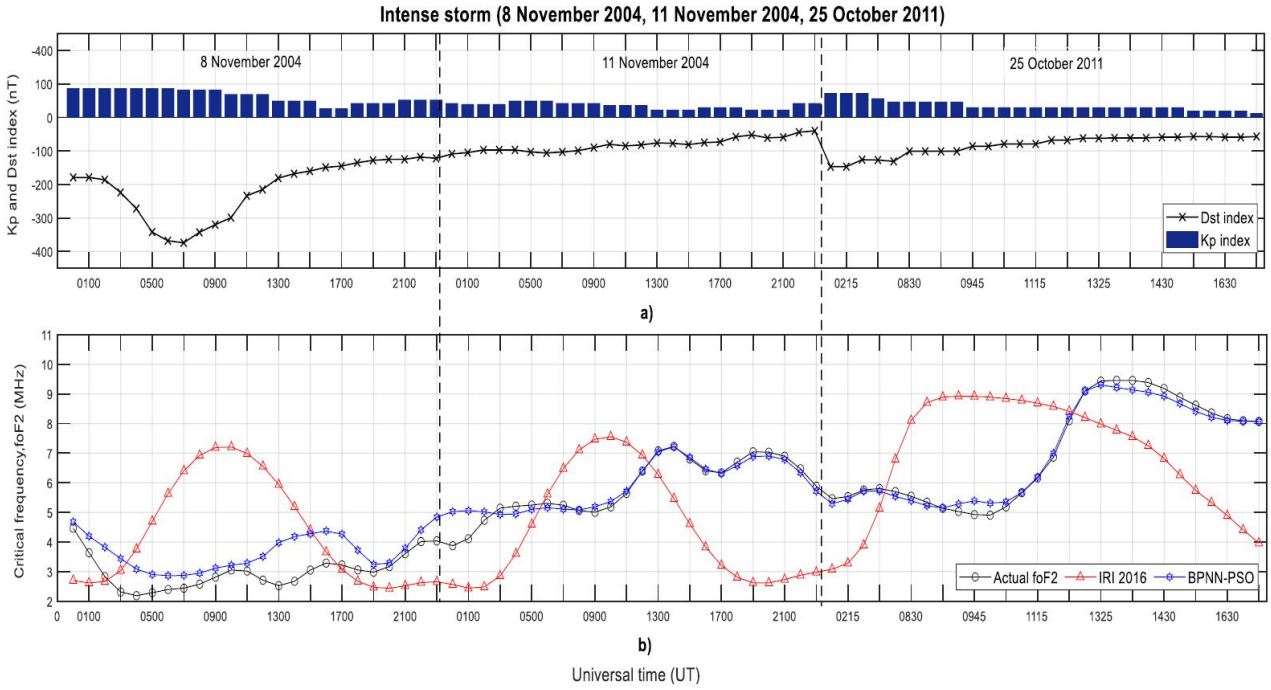

Fig. 9. Comparison of actual f_oF_2 and the models' predictions during an intense storm (8 November 2004, 11 November 2004, and 25 October 2011) (a) D_{st} and equivalent K_p indices (b) Actual (black), IRI-2016 (red), and BPNN-PSO (blue)

4. Conclusions

This paper utilized BPNN and PSO for predicting f_oF_2 during quiet and geomagnetic storm conditions. The BPNN-PSO model's predictive ability for f_oF_2 was investigated under a variety of solar activity and geomagnetic storm conditions. Moreover, this paper compared the proposed model's prediction findings with the IRI-2016 model's performance. The BPNN-PSO model outperformed the IRI-2016 model during low, medium, and high solar activity. The BPNN-PSO model had the lowest RMSE of 0.20 MHz and performed best during periods of high solar activity. The RMSE of IRI-2016 was 2.95 MHz during these times. In addition, compared with the IRI-2016 model, the BPNN-PSO model made accurate predictions during quiet and geomagnetic storm conditions. The BPNN-PSO model had the lowest RMSE of 0.54 MHz during an intense storm, whereas the RMSE of the IRI-2016 model was 2.84 MHz. The presented work can be expanded by modifying the weight and bias of the PSO algorithm during training to increase the prediction model's performance accuracy, especially under disturbed conditions.

Acknowledgment

This work was supported by the Universiti Tun Hussein Onn Malaysia under GPPS Vot No. H569. The authors thank J.H. King and N. Popitoshvili at ONET, NASA GSFC, and CDAWeb for providing the index data.

References

[1] Fan, Jieqing, Chao Liu, Yajing Lv, Jing Han, and Jian Wang. "A short-term forecast model of foF2 based on Elman neural network." *Applied Sciences* 9, no. 14 (2019): 2782. https://doi.org/10.3390/app9142782

[2] Wang, Jinlong, Guoru Ding, and Haichao Wang. "HF communications: Past, present, and future." *China Communications* 15, no. 9 (2018): 1-9. https://doi.org/10.1109/CC.2018.8456447

[3] Pietrella, M. "A short-term ionospheric forecasting empirical regional model (IFERM) to predict the critical frequency of the F2 layer during moderate, disturbed, and very disturbed geomagnetic conditions over the

European area." In *Annales Geophysicae*, vol. 30, no. 2, pp. 343-355. Göttingen, Germany: Copernicus Publications, 2012. https://doi.org/10.5194/angeo-30-343-2012

[4] Pietrella, M. "Empirical regional models for the short-term forecast of M3000F2 during not quiet geomagnetic conditions over Europe." In *Annales Geophysicae*, vol. 31, no. 10, pp. 1653-1671. Göttingen, Germany: Copernicus Publications, 2013. https://doi.org/10.5194/angeo-31-1653-2013

[5] Wang, Jian, Feng Feng, and Jianguo Ma. "An adaptive forecasting method for ionospheric critical frequency of F2 layer." *Radio Science* 55, no. 1 (2020): 1-12. https://doi.org/10.1029/2019RS007001

[6] Wang, Jian, Hongmei Bai, Xiangdong Huang, Yuebin Cao, Qiang Chen, and Jianguo Ma. "Simplified regional prediction model of long-term trend for critical frequency of ionospheric F2 Region over east Asia." *Applied Sciences* 9, no. 16 (2019): 3219. https://doi.org/10.3390/app9163219

[7] Salimov, B. G., O. I. Berngardt, A. E. Khmelnov, K. G. Ratovsky, and O. A. Kusonsky. "Application of convolution neural networks for critical frequency foF2 prediction." *Solar-Terrestrial Physics* 9, no. 1 (2023): 56-67. https://doi.org/10.12737/stp-91202307

[8] Mochalov, Vladimir, and Anastasia Mochalova. "Application of deep learning methods to predict ionosphere parameters in real time." In *E3S Web of Conferences*, vol. 196, p. 02007. EDP Sciences, 2020. https://doi.org/10.1051/e3sconf/202019602007

[9] M'Bi, Kaboré, Zerbo Jean Louis, Zoundi Christian, and Ouattara Frédéric. "Variability of the critical frequency foF2 for equatorial regions during solar Cycle's minima and maxima at Ouagadougou and manila stations." *International Journal of Geosciences* 10, no. 10 (2019): 833. https://doi.org/10.4236/ijg.2019.1010047

[10] Zhao, Jun, Xiaojun Li, Yi Liu, Xiang Wang, and Chen Zhou. "Ionospheric foF2 disturbance forecast using neural network improved by a genetic algorithm." *Advances in Space Research* 63, no. 12 (2019): 4003-4014. https://doi.org/10.1016/j.asr.2019.02.038

[11] Bai, Hongmei, Feng Feng, Jian Wang, and Taosuo Wu. "A combination prediction model of long-term ionospheric foF2 based on entropy weight method." *Entropy* 22, no. 4 (2020): 442. https://doi.org/10.3390/e22040442

[12] Yang, Zheng, Lei Qiao, Mingkun Su, Zhenhua Hu, Xuyang Teng, and Jiayi Wang. "Ionospheric foF2 nowcast based on a machine learning GWO-ALSTM model." *Advances in Space Research* 72, no. 11 (2023): 4896-4910.

[13] Zheng, Dunyong, Wusheng Hu, and Peiqing Li. "Predicting ionospheric critical frequency of the F2 layer over Lycksele using the neural network improved by error compensation technology." *Survey Review* 48, no. 347 (2016): 130-139. https://doi.org/10.1179/1752270615Y.0000000015

[14] Rawer, Karl. *Wave propagation in the ionosphere*. Vol. 5. Springer Science & Business Media, 2013. https://doi.org/10.1007/978-94-017-3665-7

[15] Abdullah, Sabirin, and Ahmad Faizal Mohd Zain. "Diurnal and seasonal variation of critical frequency in Malaysia from 2005 to 2007." *Applied Mechanics and Materials* 225 (2012): 448-452. https://doi.org/10.4028/www.scientific.net/AMM.225.448

[16] Tshisaphungo, Mpho, John Bosco Habarulema, and Lee-Anne McKinnell. "Modeling ionospheric foF2 response during geomagnetic storms using neural network and linear regression techniques." *Advances in Space Research* 61, no. 12 (2018): 2891-2903. https://doi.org/10.1016/j.asr.2018.03.025

[17] Timoçin, Erdinç, Hüseyin Temuçin, Samed Inyurt, Munawar Shah, and Punyawi Jamjareegulgarn. "Assessment of improvement of the IRI model for foF2 variability over three latitudes in different hemispheres during low and high solar activities." *Acta Astronautica* 180 (2021): 305-316. https://doi.org/10.1016/j.actaastro.2020.12.042

[18] Rao, S. S., Monti Chakraborty, R. Pandey, and A. K. Singh. "FoF2 variability at a southern low-latitude station and the performance of IRI-2016 model during ascending phase of solar cycle-24." *Advances in Space Research* 64, no. 11 (2019): 2269-2279. https://doi.org/10.1016/j.asr.2019.08.014

[19] Rao, S. S., Monti Chakraborty, and R. Pandey. "Ionospheric variations over Chinese EIA region using foF2 and comparison with IRI-2016 model." *Advances in Space Research* 62, no. 1 (2018): 84-93. https://doi.org/10.1016/j.asr.2018.04.009

[20] Thu, Hong Pham Thi, Christine Amory Mazaudier, Minh Le Huy, Dung Nguyen Thanh, Hung Luu Viet, Ngoc Luong Thi, Kornyanat Hozumi, and Thanh Le Truong. "Comparison between IRI-2012, IRI-2016 models and F2 peak parameters in two stations of the EIA in Vietnam during different solar activity periods." *Advances in Space Research* 68, no. 5 (2021): 2076-2092. https://doi.org/10.1016/j.asr.2020.07.017

[21] Asma'a, A. Hamied, and Khalid A. Hadi. "Annual behavior of electron density and critical frequency parameters during maximum and minimum years of solar cycles 22, 23 and 24." In *Journal of Physics: Conference Series*, vol. 1818, no. 1, p. 012065. IOP Publishing, 2021. https://doi.org/10.1088/1742-6596/1818/1/012065

[22] Guibula, Karim, Jean Louis Zerbo, M'Bi Kaboré, and Frédéric Ouattara. "Critical Frequency foF2 variations at korhogo station from 1992 to 2001 prediction with IRI-2012." *International Journal of Geophysics* 2019, no. 1 (2019): 2792101. https://doi.org/10.1155/2019/2792101

[23] Rumelhart, David E., Geoffrey E. Hinton, and Ronald J. Williams. "Learning representations by back-propagating errors." *nature* 323, no. 6088 (1986): 533-536. https://doi.org/10.1038/323533a0
[24] Xie, Kun, Hong Yi, Gangyi Hu, Leixin Li, and Zeyang Fan. "Short-term power load forecasting based on Elman neural network with particle swarm optimization." *Neurocomputing* 416 (2020): 136-142. https://doi.org/10.1016/j.neucom.2019.02.063
[25] Kovalick, T. "SPDF-Coordinated Data Analysis Web (CDAWeb). NASA." (2004).
[26] Atulkar, Roshni, Shivangi Bhardwaj, Prakash Khatarkar, Purushottam Bhawre, and P. K. Purohit. "Geomagnetic disturbances and its impact on ionospheric critical frequency (foF2) at high, mid and low latitude region." *American Journal of Astronomy and Astrophysics* 2, no. 6 (2014): 61-65. https://doi.org/10.11648/j.ajaa.20140206.11
[27] Wang, X., J. K. Shi, G. J. Wang, G. A. Zherebtsov, and O. M. Pirog. "Responses of ionospheric foF2 to geomagnetic activities in Hainan." *Advances in Space Research* 41, no. 4 (2008): 556-561. https://doi.org/10.1016/j.asr.2007.04.097
[28] Timoçin, Erdinç, Ali Yeşil, and İbrahim Ünal. "The effect of the geomagnetic activity to the hourly variations of ionospheric foF2 values at low latitudes." *Arabian Journal of Geosciences* 7 (2014): 4437-4442. https://doi.org/10.1007/s12517-013-1108-x